Quantum entanglement in polarization and space

Lee, Peter Sing Kin

CHAPTER 9

Mode counting in high-dimensional orbital angular momentum entanglement

We study the high-dimensional orbital angular momentum (OAM) entanglement contained in the spatial profiles of two quantum-correlated photons. For this purpose, we use a multi-mode two-photon interferometer with an image rotator in one of the interferometer arms. By measuring the two-photon visibility as a function of the image rotation angle we measure the azimuthal Schmidt number, i.e., we count the number of OAM modes involved in the entanglement; in our setup this number is tunable from 1 to 8.

M.P. van Exter, P.S.K. Lee, S. Doesburg, and J.P. Woerdman, submitted to Phys. Rev. Lett.

The most popular variety of quantum entanglement involves the *polarization* degree of freedom of two photons; in this case we deal obviously with two (polarization) modes per photon [7, 8, 23]. Recently, there has been a lot of interest in *spatial* entanglement of two photons; in this case the number of modes per photon can be much larger than two so that entanglement is correspondingly (in fact, exponentially) richer [89–91, 99–103]. This interest is motivated, fundamentally, by the desire to understand the nature of quantum entanglement in a high-dimensional Hilbert space. From the point of view of applications the high-dimensional case is important since it holds promise for implementing high-dimensional alphabets for quantum information, e.g. for quantum key distribution [104]. A popular basis for the spatial modes is the basis in which the modes are distinguished on account of their orbital angular momentum (OAM) [100–102]. An issue of much discussion in high-dimensional entanglement, OAM or otherwise, is how many modes are involved, beyond the statement that this number is (much) larger than 2 [39, 99–102, 105]. In this chapter we demonstrate a practical method to quantify the number of OAM spatial modes involved in biphoton entanglement; in our experiment this number has been varied in a controlled way from 1 to 8. This result has been achieved by using a special two-photon interferometer.

Our two-photon interferometer contains an image rotator in one of its arms (see Fig. 9.1). Similar interferometers with built-in rotation have only been tested at the *one-photon* level, where the rotation has been linked to a topological (Berry) phase [106]. A one-photon interferometer with an image reversal has been shown to act as a sorter between even and odd spatial modes [107, 108]. We will instead consider *two-photon* interference in an interferometer with built-in rotation.

In two-photon interference experiments, two photons are combined on a beamsplitter, before being detected. These experiments, which have been pioneered by Hong, Ou and Mandel (HOM) [27], demonstrate an effective bunching between the photons in each pair, but only if the optical beams have good spatial and temporal overlap. More recent versions of these "HOM" experiments study the generation of spatial anti-bunching [90], and the effect of a modified pump profile (TEM_{01} versus TEM_{00}) on the interference pattern (bunching versus anti-bunching) [89, 91].

The key question that we will address is what the observed two-photon interference in our two-photon-interferometer-with-built-in-rotation tells us about the spatial entanglement between the two multi-mode beams. As our geometry leads to an effective separation of the radial and azimuthal degrees of freedom, the experiment provides information on the entanglement between the orbital angular momenta (OAM) of the two photons [100–102]. We will show that the experiment allows to measure the azimuthal Schmidt number, i.e., it allows to count the number of entangled OAM modes.

Figure 9.1 shows a schematic overview of our two-photon interferometer. We mildly focus light from a krypton ion laser (λ=407 nm, $\theta_p = 0.50$ mrad divergence) onto a 1-mm-thick β-barium borate (BBO) crystal to generate quantum-entangled photon pairs at 814 nm via (type-I) spontaneous parametric down-conversion. These twin photons travel along the individual interferometer arms, one of them through an image rotator, before they are combined at a beam-splitter. Two-photon interference is observed by recording the number of coincidences as a function of the delay Δt between the two arms with single-photon counters (SPC). The limited detection bandwidth (5 nm) and detection angle (< 7 mrad) assure operation in the so-called thin-crystal limit [34], where phase-matching is automatically fulfilled.

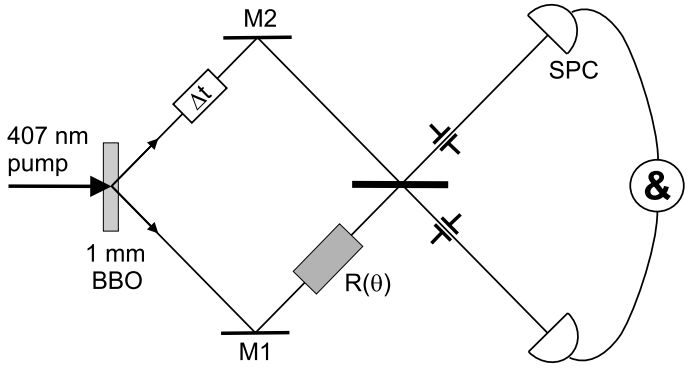

Figure 9.1: *Schematic view of the experimental setup, representing a two-photon interferometer with an image rotator $R(\theta)$ in one arm. The image rotator $R(\theta)$ consists of four out-of-plane mirrors.*

In this limit, the spatial properties of the detected two-photon field are solely determined by the pump profile.

We study the effect of an image rotation $R(\theta)$ on the two-photon interference under a symmetric TEM_{00} pump profile and for different aperture sizes, positioned approximately in the far field at $L = 1.5$ m from the crystal. The apertures allow us to control the detected number of entangled spatial modes which, together with the rotation angle θ, are the essential parameters in our experiment. We typically use an asymmetric configuration, where one circular aperture is much larger than the other and thereby effectively "fully open". We call the setup depicted in Fig. 9.1 "even", as it has an even number of mirrors in the interferometer (M1 and M2). The experimental results depicted in Figs. 9.2-9.4 have, however, been obtained with an "odd" number of mirrors (see below).

Figure 9.2 shows the measured coincidence rate as a function of the time delay Δt at a fixed rotation angle of $\theta = -30°$. The reduced coincidence rate around $\Delta t = 0$ demonstrates how two-photon interference produces an effective bunching of the two incident photons in either of the two output channels [27]. The shape of the interference pattern is the same for both geometries: its width of ≈ 260 fs (FWHM) is Fourier-related to the transmission spectrum of our filters (not shown in Fig. 1) and agrees within a few percent with the value expected for a $\Delta\lambda = 5$ nm bandwidth. The modulation depth or so-called HOM visibility, however, is quite different, being 89.5 ± 0.5 % for the 1 mm aperture and only 15.5 ± 0.5 % for the 10 mm aperture, the other aperture being "fully open" in both cases.

The reduced visibility implies a loss of entanglement and indicates the presence of spatial labeling. If the aperture size and image-rotation angle allow one to decide which of the two photons exiting the beamsplitter travelled which path in the interferometer, the two-photon interference will disappear. This discrimination can be realized by any possible imaging device (between beamsplitter and detector) and even does not need to be applied; it is sufficient if it can be done "only in principle". Experiments with an even number of mirrors always yielded visibilities close to 100% irrespective of rotation angle; apparently labeling occurs only when the total number of mirrors in the interferometer is odd.

Coincidence measurements like those presented in Fig. 9.2 were repeated for various

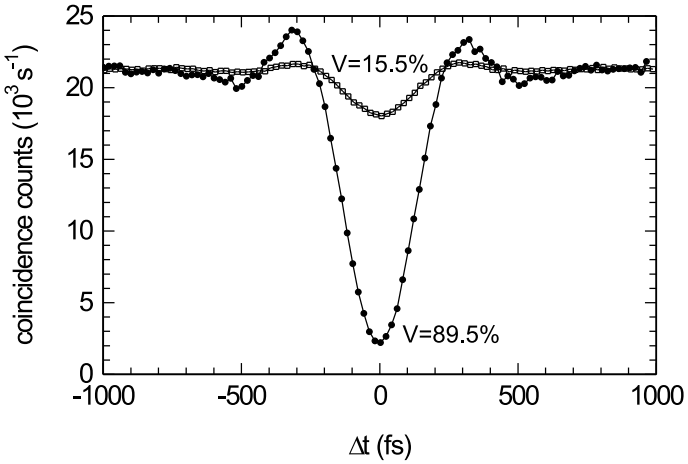

Figure 9.2: *Two-photon coincidence rate versus the time delay Δt between the two interferometer arms, measured at a fixed rotation angle of $\theta = -30^\circ$ behind a 1 mm aperture (dots) and a 10 mm aperture (squares). The coincidence rate measured for the 1 mm aperture has been multiplied by the area ratio ($\approx 100\times$) for a direct comparison with the other geometry.*

aperture sizes. Combining these results lead to Fig. 9.3, which shows the HOM visibility at a fixed rotation angle of $\theta = -30^\circ$ as a function of the aperture diameter. The drop in visibility at larger apertures illustrates the above discussion on spatial labeling. The diffraction limit imposed by the smaller apertures frustrates the observation of such labeling.

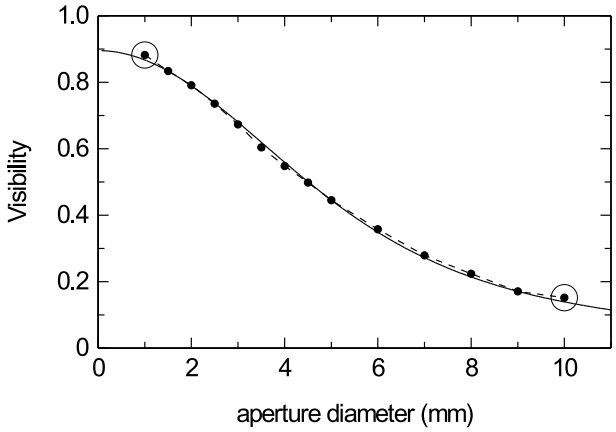

Figure 9.3: *Two-photon visibility versus the aperture diameter $2a$, measured at a fixed rotation angle of $\theta = -30^\circ$. The solid curve represents a fit. The two encircled data points correspond to the interference patterns shown in Fig. 9.2.*

By repeating the measurements shown in Fig. 9.3 for a series of *fixed rotation angles* we obtain a two-dimensional table of visibilities $V(a,\theta)$. By interchanging the rows and

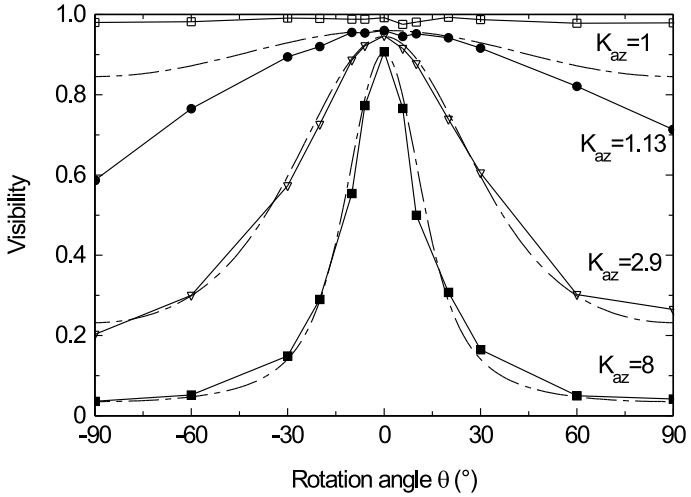

Figure 9.4: *Two-photon visibility measured as a function of the rotation angle θ behind different aperture geometries (specified by the azimuthal Schmidt number K_{az}) and behind single-mode fibers ($K_{az} = 1$). The three dashed lines have been calculated from Eq. (9.1).*

columns in this table, we now also obtain the visibility $V(\theta)$ as a function of rotation angle θ for various *fixed detection geometries*. Figure 9.4 shows these results for four different geometries, which are specified by their azimuthal Schmidt number K_{az} (see below). All curves are symmetric under the operation $\theta \leftrightarrow -\theta$ ($\theta = 0^\circ$ corresponds to no image rotation) and periodic in $\theta \leftrightarrow \theta + 180^\circ$.

For detection behind single-mode fibers (labeled as $K_{az} = 1$) the obtained visibilities of at least 98%, independent of θ. As the fundamental mode detected by these fibers is rotationally symmetric, spatial labeling and thus loss of interference will not occur under any image rotation. For free-space detection behind small apertures (small K_{az}) we observe a relatively mild effect of image rotation on the spatial entanglement. For larger apertures, this effect is much more drastic and leads to a visibility as low as 4% at $\theta = 90^\circ$ for $K_{az} = 8$. The reason for this reduction is that free-space detectors also monitor the higher-order modes. As linear combinations of these higher-order modes are no longer invariant under rotation, the correlated images at the two detectors now provide labeling information that allows one to distinguish between the interference paths followed by the two photons; a lower visibility results.

The fits in Figs. 9.3 and 9.4 are based on the following analytic expression that can be derived for the "asymmetric odd" configuration with hard-edged apertures [109]

$$V(a\sin\theta) = (1 - \exp(-\xi))/\xi \,, \tag{9.1}$$

where $\xi = 2(a/w_d)^2 \sin^2\theta$ and a is the aperture radius. The diffraction waist $w_d = 2L\theta_p$, or angular spread of one photon at a fixed position of the other, is twice the size of the pump in the (far-field) detection plane [31]. The solid curve in Fig. 9.3 is a fit based on $w_d = 1.4$ mm, in agreement with the mentioned values of L and θ_p. The three dashed curves in Fig. 9.4 are

based on the same value.

We now come to the essence of this chapter, being the question "How can we count the number of orbital angular momentum (OAM) modes involved in the high-dimensional entanglement". The answer follows directly from an expression of $V(\theta)$ in terms of OAM (or l) modes,

$$V(\theta) = \sum_l P_l \cos(2l\theta) \tag{9.2}$$

(we will derive this expression at the end of the chapter). Here P_l (with $\sum_l P_l = 1$) is the probability to detected a photon pair with orbital angular momenta $(l,-l)$ (with $-\infty < l < \infty$). Equation (9.2) shows that the observed visibility $V(\theta)$ is a weighted sum over contributions from each group of l-modes that oscillate, with their own angular dependence, between $V_l = 1$ (HOM dip) and $V_l = -1$ (HOM peak). A Fourier transformation of $V(\theta)$ directly yields the modal distribution P_l.

In order to convert the modal distribution P_l into a single number that counts the effective number of entangled OAM modes, we use the azimuthal Schmidt number as $K_{az} \equiv 1/\sum_l P_l^2$, in analogy with the general form for modal decompositions [110, 111]. The relation between the azimuthal Schmidt number K_{az} and the full 2D Schmidt number K_{2D}, where the summation runs over both azimuthal and radial mode numbers, depends on the size of the detecting apertures. For small apertures we find $K_{az} \approx K_{2D}$; for large apertures we find $K_{az} \approx 2\sqrt{K_{2D}}$ with a shape-dependent prefactor.

Based on the above description, we count the number of entangled OAM modes in our experiment in the following way: For the three lower curves in Fig. 9.4 we first performed a Fourier analysis of the normalized $V(\theta)/V(0)$ to obtain the probability distribution P_l for each curve. The azimuthal Schmidt numbers that we calculated from these distributions ranged from $K_{az} = 1.13$ for the 1 mm aperture, to $K_{az} = 2.9$ for the 4 mm aperture, and $K_{az} = 8$ for the 10 mm aperture, with many values in between. The aperture clearly allows us to tune the effective number of entangled modes.

We have repeated our measurement series for a symmetric configuration, with equal aperture sizes in front of both detectors. The general appearance of this new set of visibilities $V(\theta)$ (not shown) was similar to that measured with one aperture fully open. The small broadening of the new $V(\theta)$ profile as compared to Fig. 9.4 indicates a slight reduction in the effective mode number K_{az}.

It is instructive to also consider apertures with *Gaussian* instead of hard-edged transmission profiles ($T(r) = \exp(-2r^2/\tilde{a}^2)$), as this allows for a complete (radial and azimuthal) analytic Schmidt decomposition of the detected field, assuming two identical apertures [112]. This decomposition yields the simple Airy profile [109]

$$V(\theta) = \frac{1}{1 + (K_{2D} - 1)\sin^2\theta}\,, \tag{9.3}$$

where $K_{2D} = 1 + \frac{1}{2}(\tilde{a}/w_d)^2$ is the 2D Schmidt number. The Airy profile has almost the same shape as the function described by Eq. (9.1).

We conclude now with the promised derivation of Eq. (9.2). This is based on a description of the two-photon field as a sum over discrete spatial modes, instead of an integral over a plane-wave continuum. In this so-called Schmidt decomposition [14], the two-photon field is

represented by the pure state:

$$|\Psi\rangle = \sum_i \sqrt{\lambda_i}|u_i\rangle \otimes |v_i\rangle \ , \tag{9.4}$$

where $|u_i\rangle$ and $|v_i\rangle$ are two sets of orthonormal transverse modes. The Schmidt number $K = 1/\left(\sum_i \lambda_i^2\right)$, with $\sum \lambda_i = 1$, quantifies the effective number of participating modes.

Generally, the Schmidt decomposition of the generated field is very difficult to calculate, as its spatial extent depends both on the pump geometry and on phase matching [39, 105]. We instead consider only the relevant detected field, being the two-photon field behind the detection apertures. The Schmidt decomposition of this field is quite different and can often be done analytically [112] when the apertures are small enough to neglect phase-matching, as is the case in our experiment. The inclusion of the aperture transmission in the detected two-photon field is the key element in our present analysis.

For the rotationally-symmetric ($l = 0$) pump that we use, the symmetry of the two-photon field is such that the Schmidt decomposition of the detected field factorizes as

$$|\Psi\rangle_{in} = \sum_l \sum_p \sqrt{\lambda_{l,p}}|l,p\rangle' \otimes |-l,p\rangle'' \ , \tag{9.5}$$

where l and p are the azimuthal and radial quantum numbers and $|l,p\rangle'$ and $|-l,p\rangle''$ are the Schmidt eigenmodes of the detected field. The mentioned symmetry restricts these modes to "Laguerre-Gaussian-like" field profiles of which the precise radial distribution is co-determined by the detection apertures. As our amplitude coefficients $\sqrt{\lambda_{l,p}}$ already contain the effects of aperture filtering, they will decrease rapidly both for high p and high l values (high l-states are quite extended even for $p = 0$). A summation over the radial mode number p yields the OAM probability $P_l = \sum_p \lambda_{l,p}$.

As a last step, we propagate the two-photon field of Eq. (9.5) through our interferometer and calculate the expected two-photon visibility $V(\theta)$. This propagation will modify the two-photon field in the following ways: every mirror reflection changes the handedness by inverting the OAM of each l-state from l to $-l$. The image rotation $R(\theta)$ adds a phase factor $\exp(il\theta)$ to each l-state. The relevant beamsplitter operations are the double transmission, which leaves the l-states unaffected, and the double reflection, which swaps the labels and changes the handedness. None of these operations affect the radial component. As the detected (l,p) states form a complete orthogonal basis, two-photon interference is only observed between states with identical (l,p) labels in the detection channels. The final result is Eq. (9.2).

For a more general input state, the calculated visibility $V(\theta)$ for an interferometer with an odd number of mirrors contains terms of the form $\cos[(l_1 - l_2)\theta]$, which translate into $\cos(2l\theta)$ if we apply the conservation of OAM ($l_1 = -l_2 = l$). For an interferometer with an even number of mirrors, $V(\theta)$ contains terms of the form $\cos[(l_1 + l_2)\theta]$ instead. Our observation that $V(\theta) \approx 1$ at any angle θ in the "even-mirror geometry", can thus be interpreted as a proof of the existence of OAM entanglement; any photon pair with $l_1 \neq -l_2$ would make $V(\theta)$ angular dependent.

In summary, we have demonstrated how the high-dimensional entanglement of orbital angular momentum (OAM) can be characterized with a two-photon interferometer that contains

an odd number of mirrors and an image rotator in one of its interferometer arms. We have shown how a Fourier analysis of the observed angle-dependent visibility $V(\theta)$ profile yields the full probability distribution over the OAM modes involved in the entanglement. Finally, we have calculated the azimuthal Schmidt number K_{az} corresponding to the effective number of entangled OAM modes.

This work has been supported by the Stichting voor Fundamenteel Onderzoek der Materie (FOM).